CHAPTER

IoT for healthcare applications

8

Kamran Sayrafian[a,b], Sławomir J. Ambroziak[c,b], Dragana Bajic[d], Lazar Berbakov[e], Luis M. Correia[f], Krzysztof K. Cwalina[c], Concepcion Garcia-Pardo[g], Gordana Gardašević[h], Konstantinos Katzis[i], Pawel Kulakowski[j], and Kenan Turbic[f]

[a]*National Institute of Standards & Technology, Gaithersburg, MD, United States*
[c]*Gdańsk University of Technology, Gdańsk, Poland*
[d]*University of Novi Sad, Novi Sad, Serbia*
[e]*Institute Mihailo Pupin, Belgrade, Serbia*
[f]*INESC-ID / IST, University of Lisbon, Lisbon, Portugal*
[g]*Universitat Politècnica de València, València, Spain*
[h]*University of Banja Luka, Banja Luka, Bosnia and Herzegovina*
[i]*European University Cyprus, Nicosia, Cyprus*
[j]*AGH University of Science and Technology, Kraków, Poland*

The Internet of Things (IoT) has numerous applications in healthcare, from smart wearable or implantable sensors to remote monitoring of elderly, medical device networking, and in general creating a healthcare network infrastructure. IoT has the potential to create a pervasive environment for monitoring patients health and safety as well as improving how physicians deliver care. It can also boost patients engagement and satisfaction by allowing them to spend more time in the comfort of their residence and only interact with care centers and healthcare professionals whenever needed. A significant driver for the IoT-Health market is the increasing penetration of connected devices in healthcare. Wearable sensors have received a remarkable growth in recent years; however, a pervasive IoT-Health infrastructure is still a long way from commercialization. The end-to-end health data connectivity involves the development of many technologies that should enable reliable and location-agnostic communication between a patient and a healthcare provider.

This chapter summarizes IRACON contributions related to the application of IoT in healthcare. It consists of the following three sections. Section 8.1 presents the measurement campaigns and the related statistical analysis to obtain various channel models for wearable and implantable devices. In addition, the importance of physical human-body phantoms used for channel, Specific Absorption Rate (SAR), and Electromagnetic (EM) exposure measurements are examined. Methodologies to

[b] Chapter editors.

Inclusive Radio Communications for 5G and Beyond. https://doi.org/10.1016/B978-0-12-820581-5.00014-6

improve the accuracy of these phantoms for various frequency bands are also discussed. Section 8.2 outlines methodologies to improve the medium access control (MAC) and networking layers of a body area networks along with possible architectures for remote health monitoring. Several applications such as localization, activity recognition, and crowdsensing and their corresponding technical challenges are also presented in this section. Finally, Section 8.3 introduces the concept of nanocommunications which can be considered as the nano-scale limit of the IoT technology spectrum. It provides an overview of the promising mechanisms that can establish data communication at molecular levels inside the human body as well as various interfacing techniques with macro-scale devices. It also highlights the revolutionary healthcare applications that could be enabled by this technology.

Remark

Certain commercial equipment, instruments, or materials are identified in this chapter in order to adequately specify the experimental procedure. Such identification is not intended to imply recommendation or endorsement by the respective organizations of the chapter editors.

8.1 Wearable and implantable IoT-health technology

For wearable and implantable sensors (or actuators), there could be several communication scenarios depending on the locations of the Tx and Rx with respect to the human body. These scenarios include wireless communication among devices inside the human body (in-body-to-in-body), between an implant and a wearable device (in-body-to-on-body), between two wearable devices (on-body-to-on-body), between a wearable and an external device e.g. an off-body Access Point (AP) (on-body-to-off-body), and finally between wearable devices located on different bodies (body-to-body). The characterization and statistical modeling of these communication channels is the central topic of this section. A thorough understanding of these channels is necessary and quite important for the design and optimization of the physical and medium access layers of any communication system that involves wearable or implant devices. In the following subsections, the IRACON channel models are presented for each communication scenario.

8.1.1 Channel measurement and modeling: On-body-to-off-body

In this communication scenario, either the transmitter (Tx) or the receiver (Rx) is a wearable device, while the other communicating node is at a fixed location away from the human body. Although this scenario may seem similar to use-cases including a mobile personal device, the impact of the human body on the antenna operation as well as the strong influence of the user dynamics on the communication link are among the distinguishing features that necessitate a dedicated channel model.

Analytical model

Turbic et al. have proposed a polarimetric geometry-based off-body channel model [TCB19] based on Geometrical Optics (GO) and Uniform Theory of Diffraction (UTD). The model also considers arbitrary antenna positions, orientations and radiation characteristics, i.e. polarization and gain. The transmission coefficient (h_{ch}) of a narrowband channel is represented as:

$$h_{ch} = \frac{\lambda}{4\pi} \sum_{n=1}^{N_m} \frac{1}{r_n} \mathbf{g}_r^H(\phi_r^n, \psi_r^n)_{[1\times 2]} \mathbf{H}_{p\,[2\times 2]}^n \mathbf{g}_t(\phi_t^n, \psi_t^n)_{[2\times 1]} e^{-j\frac{2\pi}{\lambda} r_n} \tag{8.1}$$

where λ is the wavelength, N_m is the number of MPCs, r_n is the n-th path length, $\mathbf{g}_{t/r}$ is the polarimetric gain vector of the Tx/Rx antenna, $\phi_{t/r}^n$ and $\psi_{t/r}^n$ are the azimuth and elevation angles at the Tx/Rx respectively, and $\mathbf{H}_n$ is the path polarization matrix.

The polarization matrices differ for the LOS component ($\mathbf{H}_0$) and the reflected MPCs ($\mathbf{H}_n$) as follows:

$$\mathbf{H}_{0\,[2\times 2]} = \mathbf{Q}(\theta_{LOS})_{[2\times 2]} \tag{8.2}$$

$$\mathbf{H}_{n\,[2\times 2]} = \mathbf{Q}(\theta_r^n)_{[2\times 2]}\, \mathbf{\Gamma}_r(\theta_i^n)_{[2\times 2]}\, \mathbf{Q}(\theta_t^n)_{[2\times 2]} \tag{8.3}$$

where $\mathbf{Q}$ represents rotation matrix, $\mathbf{\Gamma}_r$ is the reflection matrix, θ_{LOS} is the polarization reference mismatch angle in the LOS direction, θ_i^n incidence/reflection angle, and $\theta_{t/r}^n$ is the mismatch angle between the polarization references associated with the Tx/Rx antenna and with the reflection/incidence plane. The angles θ_{LOS}, $\theta_{t/r}^n$ and θ_i^n are obtained from the scenario geometry as detailed in [TCB19, App. A].

To consider the human body dynamics, an analytical mobility model for the wearable antenna has been developed in [TCB18]. The model represents antenna motion as a composition of a linear forward motion at constant velocity, and a periodic component. This is illustrated in Fig. 8.1a. The antenna position over time ($\mathbf{r}$) is therefore represented by:

$$\mathbf{r}_{[\mathrm{m}]}(t) = \mathbf{r}_{0\,[\mathrm{m}]} + v_{u\,[\mathrm{m/s}]} t_{[\mathrm{s}]}\, \mathbf{u}_v + \Delta\mathbf{r}_{[\mathrm{m}]}(t) \tag{8.4}$$

where v_u is the user's velocity, $\mathbf{r}_0$ is the starting point, $\mathbf{u}_v$ is the unit direction vector, and $\Delta\mathbf{r}$ represents the periodic displacement due to the changing posture. The corresponding orientation is represented by Euler angles, i.e. γ_1, γ_2, and γ_3, which specify a sequence of elementary rotations around the local coordinate axes Z-Y-Z, respectively. This will establish the orientation of the associated local coordinate system [TCB18, Eqn. 10-12]. The relation between the global and local coordinate systems is illustrated in Fig. 8.1b, where the rotation axes and the corresponding angles have also been indicated.

Due to the periodic changes in the human posture during walking or running, the periodic position component in (8.4) and the Euler angles are modeled by a Fourier series with up to two harmonics [TCB18, Eqn. 9,13]. The corresponding parameters are calculated from Motion Capture (MoCap) data [TCB18, Tab. 1].

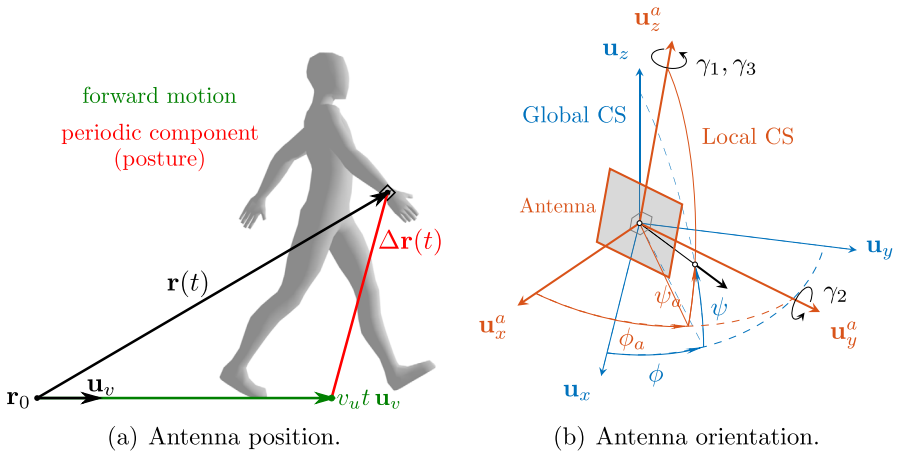

(a) Antenna position. (b) Antenna orientation.

FIGURE 8.1

Wearable antenna mobility model.

The scattering environment surrounding the human body is represented by a simplified geometry i.e. scattering is assumed to occur on a circular cylinder centered around the body. This simplification is adopted to allow simultaneous consideration of multiple wearable antennas on the body. In other words, the scatterers are assumed to be fixed with respect to the human body; however, their impacts on different on-body antennas will depend on the relative positions of the antennas with respect to the scatterers.

The channel model was used to investigate the effects of different aspects of antenna motion in [TC20a]. A significant impact of user's motion on the polarization characteristics was observed, and the error in average cross-polarization ratio exceeded 23 dB when the antenna dynamics were neglected.

The antenna rotation has a dominant effect on the polarization matrix. However, the corresponding periodic displacement due to changing posture can be neglected. This allows for further simplification of the model. On the other hand, the antenna displacement has a significant impact on the small-scale fading characteristics. The fading dynamics are observed to vary over the motion period with distinct slow and fast phases [TC20b]. The latter is observed to result in 4 times higher Level-Crossing Rate (LCR) than the former when the antenna is located on the lower leg.

The channel model was validated against measurements, and a good agreement with the experimental data was observed. Using narrowband measurements data at 2.45 GHz [TAC17,ACK+16], the model's capability to reproduce polarization characteristics and temporal dynamics of the signal was demonstrated in [TCB19]. A good agreement with wideband measurements at 5.8 GHz [TACB18,TACB19] was also reported in [ATC19], and simulation error in the received power was shown to be within 3 dB. Fig. 8.2 shows the comparison between simulation (sim.) and measure-

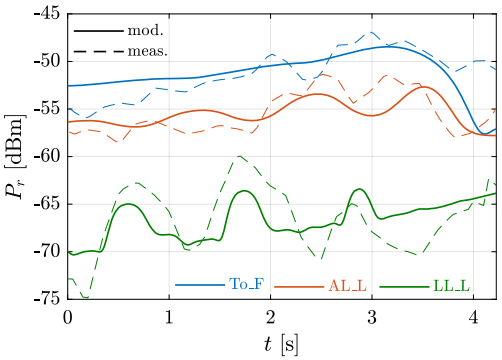

FIGURE 8.2

Comparison between the simulated and measured Rx power, for vertical off-body antenna polarization.

ments (meas.) for a scenario where the user is walking toward a vertically polarized AP antenna, while wearing antennas on the chest (To), wrist (AL), and lower leg (LL).

The wearable antenna rotation during motion was observed to strongly affect the antenna gain and polarization characteristics relative to the fixed off-body antenna, resulting in time-variant polarization losses [TCB17]. Therefore, the on-body antenna placement plays an important role on the off-body channel characteristics. Antennas on the arms and legs result in more severe Rx signal variations compared to locations such as the chest and head [TCB19].

Empirical models

The most common statistical path loss model based on narrowband measurements is[1]

$$L_{pl}(d,t)_{[\mathrm{dB}]} = \overline{L_{pl}(d)}_{[\mathrm{dB}]} + \Delta L_{ls}(t)_{[\mathrm{dB}]} + \Delta L_{ss}(t)_{[\mathrm{dB}]} \tag{8.5}$$

where t denotes time, d is the Tx-Rx distance, $\overline{L_{pl}}$ is Mean Path Loss (MPL), ΔL_{ls} and ΔL_{ss} are the large- and small-scales fading components. A standard log-distance model is also typically adopted for the MPL component, i.e.

$$\overline{L_{pl}(d)}_{[\mathrm{dB}]} = \overline{L_{pl}(d_0)}_{[\mathrm{dB}]} + 10\, n_{pl} \log\left(\frac{d}{d_0}\right) \tag{8.6}$$

where n_{pl} is the path loss exponent, and d_0 denotes the reference distance (e.g. 1 m). The fading components are modeled by random variables with distributions that are derived from statistical analysis of the measurements.

[1] By adopting the common practice in literature, the term path loss is used loosely herein. Due to the inability to de-embed the antennas from signal measurements, the measured loss actually corresponds to attenuation between antennas' terminals, i.e. system loss by definition [ITU16].

The data processing procedure used for the path loss component extraction and the estimation of model parameters is typically as follows. The small-scale fading variations are first eliminated from the instantaneous path loss by a moving average filter with an averaging distance of 10λ, the latter being a typical choice for indoor measurements [VLJ97]. After extracting small-scale fading, the log-distance model (8.6) is fitted to the remaining signal which includes a combination of MPL and large-scale fading.

With the path loss decomposed according to (8.6), a statistical analysis of large- and small-scales fading is performed for parameter selection. Commonly considered Goodness of Fit (GoF) tests for evaluation of different candidates are Akaike Information Criterion (AIC) [BA02], χ^2 and correlation tests [PP02]. One should note that the model parameters are usually provided separately for LOS, Quasi-LoS (QLOS), and NLOS conditions.

The large-scale fading is commonly reported to have a Lognormal distribution, while Rice, Nakagami-m, Rayleigh, and Lognormal distributions are the typical models used for small-scale fading. The latter is found to primarily depend on body-shadowing conditions and antennas' polarization. Moreover, the model parameters could vary with frequency, environment, antennas' radiation characteristics, and their on-body placement. The path loss model parameters reported to IRACON are summarized in Tables 8.1 and 8.2, and the corresponding experimental studies are briefly described in the following.

Table 8.1 Summary of MPL and Lognormal large-scale fading parameters in off-body channels.

n_{pl}	$\overline{L_{pl}(d_0)}_{[\mathrm{dB}]}$	$\mu_{L\,[\mathrm{dB}]}$	$\sigma_{L\,[\mathrm{dB}]}$	$f_{[\mathrm{Hz}]}$	Env.	Ref.
1.71	[32, 50]	0	[1.2, 3.0]	2.45 G	Office	[TAC17]
-	-	0	[1.4, 2.0]	2.45 G	Office	[WA19]
1.69	[25.2, 64.7]	0	[1.7, 6.5]	2.45 G	Ferry*	[KAS+18]
-	-	0	[1.2, 2.9]	2.45 G	Ferry†	[KACS19]
[0.16, 3.80]	[64.7, 76.2]	[-0.2, -0.4]	[2.0, 2.6]	868 M	Ferry‡	[CAR18a]
[0.13, 3.46]	[23.4, 30.7]	-0.3	[2.2, 2.8]	6.5 G	Ferry‡	[CAR18a]

Dome-shaped discotheque; †straight corridor; ‡L-shaped corridor

Narrowband measurements

The parameters in Tables 8.1 and 8.2 were obtained through several measurement campaigns, performed in different environments. Ambroziak and Turbic et al. [ACK+16,TAC17,ATC17] reported measurements results at 2.45 GHz, in a typical indoor office environment, while considering static, quasi-dynamic, and dynamic user scenarios. In static and quasi-dynamic scenario (i.e. with the user moving in place) different orientations of the user (leading to LOS, QLOS, and NLOS conditions) were considered. The dynamic scenario had the user walking towards and away from the off-body antenna, over a straight path.

Table 8.2 Summary of small-scale fading parameters in off-body channels.

Dist.	Parameters		$f_{[\mathrm{Hz}]}$	Env.	Ref.
Nakagami[1]	$m_{Nk} \in [0.9, 19.5]$	$\Omega_{Nk} \in [1.0, 2.0]$	2.45 G	Office	[TAC17]
Rice[2]	$s_{Ri} \in [0.8, 1.0]$	$\sigma_{Ri} \in [0.5, 0.7]$	2.45 G	Office	[WA19]
Nakagami[1]	$m_{Nk} \in [0.8, 1.5]$	$\Omega_{Nk} \in [1.5, 2.1]$	2.45 G	Ferry*	[KAS+18]
Nakagami[1]	$m_{Nk} \in [0.8, 0.9]$	$\Omega_{Nk} \in [1.9, 2.2]$	2.45 G	Ferry†	[KACS19]
Lognorm.[3]	$\mu_{Ln\,[\mathrm{dB}]} = -0.4$	$\sigma_{Ln\,[\mathrm{dB}]} \in [2.1, 2.2]$	868 M	Ferry‡	[CAR18a]
Lognorm.[3]	$\mu_{Ln\,[\mathrm{dB}]} = -0.3$	$\sigma_{Ln\,[\mathrm{dB}]} \in [1.5, 1.7]$	6.5 G	Ferry‡	[CAR18a]

*Dome-shaped discotheque; †straight corridor; ‡L-shaped corridor
[1] m_{Nk} (shape) and Ω_{Nk} (scale); [2] s_{Ri} (noncentrality) and σ_{Ri} (scale); [3] μ_{Ln} (log-mean) and σ_{Ln} (log-standard deviation)

The measurements were repeated with co-polarized [ACK+16] and cross-polarized antennas [TAC17]; therefore, providing a data set for channel characterization and estimation of model parameters in orthogonal polarizations. An alternative approach to estimate the MPL model parameters was proposed in [TAC17,ATC17]. The authors calculated the path loss exponent for the LOS case in the co-polarized channel, and estimated the intercept term $\overline{L_{pl}(d_0)}$ in (8.6) for each scenario.

The large-scale fading was reported to follow a lognormal distribution, while Nakagami-m was the best overall statistical model for small-scale fading. Parameters of the Nakagami distribution were found to be considerably different in the co- and cross-polarized channels. The distribution was closer to Rice and Rayleigh, respectively in the former and latter case.

Another set of measurements in the same environment and at the same frequency were performed by Wiszniewski and Ambroziak [WA19]. However, the scenario involved the user passing by an off-body antenna that was placed at a fixed distance from the user's walking path. Various on-body antenna placements such as chest, back, wrist, and head were considered in this measurement. Lognormal and Rice distributions were reported as the best model for large- and small- scale fading components respectively.

In order to avoid MPL model parametrization for each user orientation, Turbic et al. [TAC18a] have introduced an additional term to (8.5) to account for the orientation-dependent body-shadowing loss, i.e. shadowing pattern (S_{sh}), given by:

$$S_{sh}(d,\phi)_{[\mathrm{dB}]} = S_m(d)_{[\mathrm{dB}]}\,\frac{1}{2}\left\{1+\cos\left[\frac{2\pi}{\Delta\phi}(\phi-\phi_0)\right]\right\} \tag{8.7}$$

where ϕ is the azimuth angle of arrival/departure at the wearable antenna, S_m is the distance-dependent maximum body-shadowing loss, ϕ_0 is the azimuth angle of maximum loss, and $\Delta\phi$ is the shadowing pattern angular width. The model parameters were obtained from the indoor measurements at 2.45 GHz [TAC18a, Table I], with the user rotating at different distances from the off-body antenna. Fig. 8.3 shows the shadowing pattern (8.7) that is fitted to the measurement data. While the general

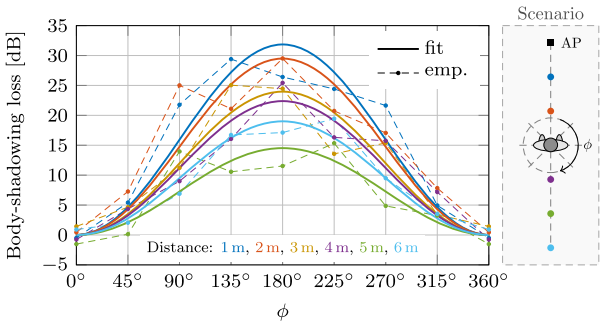

FIGURE 8.3

Body-shadowing loss as a function of user orientation.

model is applicable for on-body-to-off-body and body-to-body channels, additional measurements are required to estimate the parameters for the latter case.

In addition to typical indoor environments, measurements were also conducted in a passenger ferryboat [KAS+18,CAR18a,KAC17], where various metal structures could result into strong signal reflections. Authors in [KAS+18] have performed narrowband measurements at 2.45 GHz inside a dome-shaped discotheque within the ferryboat. They considered a scenario where the user walks towards and away from an AP at a fixed position. The measurements were obtained in two orthogonal polarizations, and repeated for wearable antennas located on the arm, chest, and head.

While the authors adopted the same MPL model (8.6), an additional term (L_{pa}) was introduced in (8.5), in order to take the effects of the wearable antenna height and orientation into account, i.e.

$$L_{pa\,[\mathrm{dB}]} = 10\,a \log |\Delta h_{[\mathrm{m}]}| + b_{[\mathrm{dB}/^\circ]}\mu_{\phi\,[^\circ]} + c_{[\mathrm{dB}/^\circ]}\sigma_{\phi\,[^\circ]} \tag{8.8}$$

where Δh is the difference in Tx and Rx antennas' heights, a, b, and c are the model parameters, μ_ϕ is the mean angle in between the walking direction and the maximum on-body antenna radiation, and σ_ϕ is the corresponding standard deviation (Table 8.3). The statistical analysis performed by the authors shows that the best models for large- and small-scales fading in this environment are Lognormal and Nakagami-m distributions, respectively,

Table 8.3 Model parameters for L_{pa} [KAS+18].

a	b	c	Δh	μ_ϕ	σ_ϕ
[-1.06, 0.79]	[0.0, 0.1]	[-3.3, -1.4]	[0.05, 0.45]	[-97.0, 69.9]	[2.6, 5.2]

Considering the same scenario and settings, the authors also performed additional measurements at 2.45 GHz in a straight corridor within the same ferry [KACS19]. The same statistical models (with different values of parameters) were reported to fit this environment as well (Table 8.2).

Authors in [CARC17,CAR18a] have performed measurements in an L-shaped corridor with the user walking toward and away from an AP placed in one leg of the corridor. LOS and NLOS conditions were distinguished depending on whether the user and the AP are in the same leg of the corridor. Using a custom-developed dual-band measurement stand, the data were simultaneously recorded at 868 MHz (narrowband) and in the 6489 MHz UWB channel. The embedded UWB radio module was additionally used to associate each sample with the corresponding Tx-Rx distance. The measurements were repeated for the same wearable antenna placements as in [KAS+18], i.e. the head, chest, and wrist. An example of the measured path loss for this scenario is shown in Fig. 8.4, which also illustrates LOS/NLOS classification and shows the MPL model fitted to the data.

The authors have reported the Lognormal distribution as the best fitting model for large-scale fading. This also agrees with other studies presented here. On the other hand, in contrast to the other reports, the authors found that the small-scale fading also follows a Lognormal distribution.

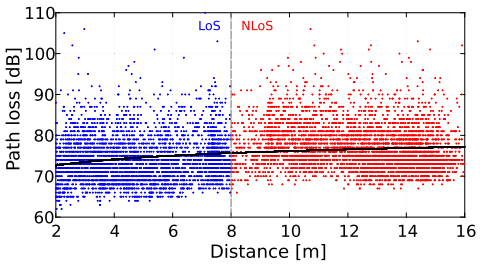

FIGURE 8.4

MPL model fitted to measurements in a ferry (L-shaped corridor).

In [KAC17], Kosz et al. have performed measurements with the user sleeping in a passenger cabin. In their study, narrowband measurements at 2.45 GHz were performed simultaneously with two wearable antennas. The wearable antennas were placed on the chest and back side of the user in one configuration, and the chest and wrist in the other. The data was obtained with two types of wearable antennas, namely FlexPIFA and FlexNotch. The authors reported the Rx mean power and standard deviation. The mean power was found to vary between 56 dB and 70 dB over the considered scenarios, while the variation of the standard deviation was between 3.7 dB and 8.0 dB. A strong dependence of these parameters on the user's orientation, type of the wearable antenna and its placement was observed; however, the height at which the user slept inside a bulk bed showed little impact on the results.

Wideband measurements

While most of the empirical contributions to IRACON considered narrowband fading channels, authors in [TACB18,TACB19] reported the results of dual-polarized CIR measurements at 5.8 GHz, with 500 MHz bandwidth, conducted in an indoor environment The measurement campaign included a number of different scenarios designed

to investigate the influence of depolarization, user dynamics, body-shadowing from the user or another person, as well as the scattering impact of people in the environment around the user [TACB18]. The measurements were obtained simultaneously with orthogonally polarized antennas, and repeated for antenna placement on the chest, wrist, and lower leg. Results show strong influence of the user dynamics and body-shadowing on the CIR parameters, i.e. number of paths, Rx power, and delay spread; therefore, leading to an effectively non-stationary channel [TACB19]. The ratio of the received powers in the orthogonal polarization was found to vary up to 21.3 dB when the user walks toward or away from the antenna.

Another set of CIR measurements over the UWB frequency range 3.8-10.2 GHz was reported by Wilding et al. [WMW19], and provided an insightful analysis of the body-shadowing effect and off-body channel characteristics under obstructed LOS conditions. A significant pulse distortion and widening due to attenuation and body-diffracted waves was observed. The attenuation of the LOS component due to the body-shadowing is characterized by introducing the effective energy pattern of a wearable antenna, i.e. Rx power distribution over azimuth angles relative to the maximum radiation direction. Fig. 8.5 shows this pattern for different antenna placements indicated in the figure, with the free-space antenna scenario being also provided for reference.

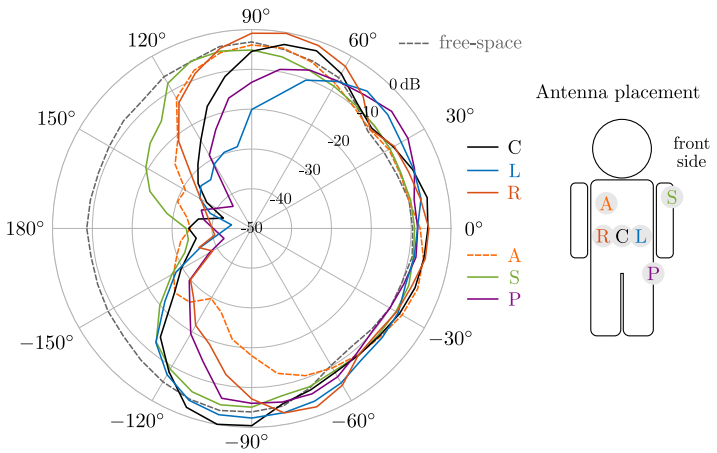

FIGURE 8.5

Wearable antenna effective energy pattern.

Millimeter-wave measurements

While all of the empirical studies discussed so far consider frequencies below 6.5 GHz, two off-body channel measurement campaigns at centimeter- and millimeter-waves were also reported to IRACON [SPCN18,ZGL+17]. Sana et al. [SPCN18] reported wideband off-body channel measurements at 60 GHz, obtained by using a channel sounder developed at Durham University (UK). While only the

initial results based on visual inspection of the measured CIR were presented, the authors also investigated the achievable diversity gains by employing a 2×2 MIMO antenna, and considering three different combining techniques.

Zhao et al. considered outdoor mobile off-body channel at 15 GHz and 28 GHz [ZGL+17]. The impact of the human body on the radiation characteristics of mobile terminals was investigated by evaluating the radiation efficiency reduction and gain pattern distortion due to blockage. The study was carried out for three types of antennas: notch, slot, and edge-patch antenna. According to the reported results, the radiation efficiency reduction due to body proximity is up to 4 dB lower at 15 GHz and 28 GHz, than at frequencies below 6 GHz. By using the measured mobile antenna radiation patterns in ray-tracing simulations, the coverage areas at 15 GHz and 28 GHz were compared for an urban pedestrian scenario. The latter frequency was reported as lass favorable due to higher path loss and body-blockage losses.

Finally, the empirical studies reported to IRACON also addressed the body-to-body communication scenario as a special case of the off-body communication. A narrowband measurement campaign at 2.45 GHz performed in indoor and outdoor environments was reported in [ACT16a]. The experiment considered scenarios where the users walking toward and away from each other, as well as walking in parallel. The large- and small-scales fading were found to follow Lognormal and Nakagami-m distributions, respectively, similar to the off-body channels with fixed APs [TAC18b]. Body-shadowing was observed to strongly affect the small-scale fading characteristics. The average amount of fading (fading merit) was up to 2.56 times higher when LOS is obstructed. The environment was also found to have a significant impact as well. The small-scale fading was observed to be more severe in the indoor environment i.e. 1.88 times higher average fading and 3.81 dB lower K-factor.

8.1.2 Channel measurement and modeling: On-body-to-on-body

For body surface communication, antenna orientation and polarization with respect to the environment is an important issue that is sometimes ignored in path loss calculation. This issue could be particularly significant in dynamic scenarios where the person wearing the antenna is in motion.

Authors in [Aoy16] took antenna directivity into consideration for Body Area Networks (BANs) using millimeter or terahertz frequencies. In their research, variation in the direction of on-body antennas and the frequent occurrence of body-shadowing in dynamic scenarios have been highlighted. The temporal variation of the azimuth and zenith angles of the on-body antennas and shadowing rate is investigated using simulation. Antenna placements considered in their study included possible wearable applications such as abdomen, chest, head, upper arm, ankle, thigh, and hand. Results show that in some scenarios, azimuth and zenith angles of the antenna exhibit a large variation during a person's walk. Therefore, high speed beamforming mechanisms should be considered if the on-body antenna has high directivity.

8.1.3 Channel measurement and modeling: In-body-to-on-body and in-body-to-off-body

As mentioned earlier communication with an implant device could include three scenarios i.e. communication between two implants (in-body-to-in-body), between an implant and an on-body device (in-body-to-on-body), and between an implant and an off-body device (in-body-to-off-body). Radio wave propagation from an implant device is highly affected by the dielectric properties of the human body tissues on its path. These properties impact both the antenna characteristics (e.g. matching, radiation pattern) and the propagation channel. In the following subsection, implant communication channels in the human body or an animal are discussed.

Human body implants

Two different MPL models are proposed for these channels: a log-linear model similar to Eq. (8.5) but with reference distance d_0 of 1 cm, and a linear model as the following:

$$\overline{L_{pl}(d)}_{[\text{dB}]} = \overline{L_{pl}(d_0)}_{[\text{dB}]} + \alpha_{pl\,[\text{dB/cm}]}\, d_{[\text{cm}]} \tag{8.9}$$

where α_{pl} is the slope, and $\overline{L_{pl}(d_0)}$ is the MPL at zero distance.[2]

The path loss variations around the MPL are found to exhibit Lognormal distribution similar to the off-body channel.

The parameters of the models are summarized in Tables 8.4 and 8.5 for all three channel scenarios. The parameters values were derived from numerical full-wave simulations, wideband measurements using physical phantoms and *in vivo* experiments. For the liquid phantom experiment [AGF+16], one antenna was fixed at a specific location and the other was moved over a spatial grid in order to collect sample measurements. The in-body-to-off-body channel was investigated based on *in vivo* and phantom-based measurements reported in [GFA+16]. There are several studies contributing to the in-body-to-on-body channel model parametrization [AGF+16,GFA+16,AGC+18,PSAGP+19]. The phantom-based measurements were reported in all studies, and the *in vivo* measurements have been reported in [GFA+16,PSAGP+19].

The measurements obtained with the liquid phantoms are observed to generally overestimate the path loss, specially when the distance between the antennas increases. Therefore, a correction model can be applied to the set of available phantom-based measurements for more realistic path loss estimates [GFA+16]. The distance-dependent correction factors (C_{pl}) for the linear (8.5) and log-linear (8.9) MPL models are given by (8.10) and (8.11) respectively:

$$C_{pl}(d)_{[\text{dB}]} = 1.1 + 7.4\,\log(d_{[\text{cm}]}) \tag{8.10}$$

$$C_{pl}(d)_{[\text{dB}]} = 5.8 + 2.2\,d_{[\text{cm}]} \tag{8.11}$$

[2] This is a control point of the model without a meaningful physical interpretation, as the model is not applicable for co-located antennas.

Table 8.4 Log-linear MPL model parameters and standard deviations in channels with implants.

Ch.	$\overline{L_{pl}(d_0)}_{[\text{dB}]}$	n_{pl}	$\sigma_{Ln\,[\text{dB}]}$	$d_{[\text{cm}]}$	$f_{[\text{GHz}]}$	Ref.
in2off	[70.4, 71.5]	[0.7, 1.4]	-	4 - 50	3.1 - 8.5	[GFA+16]
in2on	47.8	1.98	1.2	5.5 - 20	3.1 - 8.5	[AGF+16]
	[-12.2, 35.8]	[5.8, 9.3]	[5.0, 5.7]	2.8 - 8	3.1 - 5.1	[AGC+18]
	[-29.7, 26.2]	[5.4, 10.3]	[2.0, 4.6]	2.8 - 8	3.1 - 5.1	[PSAGP+19]

Table 8.5 Linear MPL model parameters and standard deviations in channels with implants.

Ch.	$\overline{L_{pl}(d_0)}_{[\text{dB}]}$	$\alpha_{pl\,[\text{dB/cm}]}$	$\sigma_{Ln\,[\text{dB}]}$	$d_{[\text{cm}]}$	$f_{[\text{GHz}]}$	Ref.
in2in	45	4.6	4.3	3 - 8	3.1 - 8.5	[AGF+16]
in2on	[30.8, 36.6]	[5.2, 7.4]	-	3 - 11	3.1 - 5.0	[GFA+16]
	[14.8, 53.4]	[4.5, 7.4]	[5.0, 5.7]	2.8 - 8	3.1 - 5.1	[AGC+18]
	[13.8, 41.6]	[4.3, 6.8]	[2.0, 4.6]	2.8 - 8	3.1 - 5.1	[PSAGP+19]

Animal implants

In addition to health monitoring applications in humans, implants can also be used in animals, for example tracking the health conditions of dairy cows and facilitating herd management. Benaissa et al. in [BPN+19] presented the in-body-to-off-body path loss between an implanted device inside a cow and an external node. The proposed model was obtained based on measurements conducted with several cows in a 6 m × 18 m barn, housing seven fistulated dairy cows. The authors adopted the statistical path loss model (8.5) and fitted the MPL model (8.6) to the measurement data. The large- and small-scales fading components (ΔL_{ls} and ΔL_{ss}) were considered jointly and assumed to have a zero-mean Gaussian distribution with standard deviation $\sigma_{[\text{dB}]}$. The reported MPL model parameters are summarized in Table 8.6.

Table 8.6 MPL model parameters for in-body-to-off-body channels with animal implants.

$\overline{L_{pl}(d_0)}_{[\text{dB}]}$	n_{pl}	$\sigma_{[\text{dB}]}$	$d_{[\text{m}]}$	$f_{[\text{MHz}]}$	Ref.
[48.3, 98.5]	[1.9, 2.1]	[1.8, 4.9]	1 - 20	433	[BPN+19]

Using the proposed channel model, the authors also calculated the expected transmission range for LoRa technology. Depending on the Tx power and the desired data rate, it was shown that a transmission range of up to 100 m could be achieved.

8.1.4 Human body phantoms and SAR measurement

Analysis of the exposure of the human body to electromagnetic waves is an important field of research for IoT applications in healthcare. The goal in this research is to

evaluate the impact of the electromagnetic fields on the human health. RF exposure tests focus on confirming that the maximum allowable absorption rate is not exceeded by the regulatory limits. To carry out such tests, it is also important to know the electromagnetic properties of the human body tissues.

The electromagnetic properties of the body tissues are expressed in terms of their permittivity and permeability. Since the human body is a non-magnetic medium, the permeability of its tissues is equivalent to that of the air. In contrast, the permittivity varies considerably for different body tissues. This is especially the case at Gigahertz frequencies and above. The relative permittivity which is the absolute permittivity normalized to that of the air, ε_r^*, is a complex frequency-dependent property. The real part of the relative permittivity (ε_r') is the dielectric constant, and its imaginary part (ε_r'') is the loss factor. Therefore, relative permittivity can be expressed as: $\varepsilon_r^*(f) = \varepsilon_r'(f) - j\varepsilon_r''(f)$. In some cases, the imaginary part of the permittivity is given as the dielectric conductivity that can be deduced from the loss factor i.e. $\sigma(f) = 2\pi f \varepsilon_r''(f)\varepsilon_0$, where ε_0 is the relative permittivity of the vacuum.

Both dielectric constant and loss factor (or conductivity) define the behavior of the electromagnetic waves traveling through different human body tissues. Therefore, it is important to consider the values of the complex permittivity in the study of implant propagation channels. The most widely used repository of such values was given by C. Gabriel in [Gab96] more than 20 years ago. It provides the values of the dielectric constant and loss factor as a function of frequency (from several kHz to GHz). However, researchers should take into account that Gabriel's repository was produced from experiments in different animal species using various measurement techniques.

In all IoT use-cases involving implants, laboratory measurements and/or software simulations are necessary in order to evaluate the performance of the wireless link in the human body environment. Researchers should use hardware or software models that replicate the complex permittivity of the tissues involved in the study. These kinds of models are referred to as *phantoms*. They are intended to accurately emulate electrical properties of different body tissues.

Dielectric properties of body tissues

There are several methods for measuring the dielectric properties of any material. Open-ended coaxial probe, transmission lines, resonant cavities or parallel plates are the most known methodologies reported in the literature. The requirements of the measurement, the type of material and the frequency range determine which kind of methodology is the most useful in each case. In particular, the open-ended coaxial probe is the most used technique for measuring the electromagnetic properties of body tissues. It allows broadband measurement for liquids, gels or semisolids with high accuracy. This approach is based on a rigid coaxial cable with a flat cut end (open-ended coaxial) submerged into the liquid or posed over the surface of the gel or semisolid. The probe is connected to a Vector Network Analyzer (VNA) which is responsible for measuring the values of the reflection coefficient (scattering parame-

ter $S_{11}(f)$) for all frequencies under analysis. Next, the $S_{11}(f)$ values are translated into their corresponding dielectric constants i.e. $\varepsilon_r'(f)$, and loss factor, $\varepsilon_r''(f)$.

Considering the open-ended coaxial technique, an adequate prior calibration of the probe is the key in order to obtain accurate values of both dielectric constant and loss factor. In the literature, several calibration procedures have been addressed so far. The most common procedure consists of measuring the reflection coefficient of at least three different elements (known as reference standards) with well-known complex permittivity. The most used reference standards are open circuit, short circuit, and water (hereinafter called "typical calibration") since their dielectric properties are well reported in the literature. However, in [FLGPC+17], authors demonstrate that these standards are not the most appropriate when measuring high water-content body tissues such as muscle, heart, stomach, and liver. For these cases, the lowest uncertainty of the measurements was achieved by adding methanol to the three calibration standards used in the typical calibration, i.e. by using an open circuit, short circuit, water, and methanol. This is due to the fact that the complex permittivity of methanol is at the same order of magnitude as that of the high water-content tissues. This effect can be observed in Fig. 8.6 where authors measure a liquid with permittivity similar to that of the high water-content tissues i.e. Dimethyl sulfoxide (DMSO). Authors also considered the typical calibration as well as methanol, ethanol, and 2-propanol as additional calibrators. The lowest values of the measurement uncertainty for the complex permittivity values was achieved by adding methanol to the calibration standards. For low water-content body tissues, authors in [FLGPC+17] reported that ethanol is also the best additional calibrator and provides the lowest uncertainty.

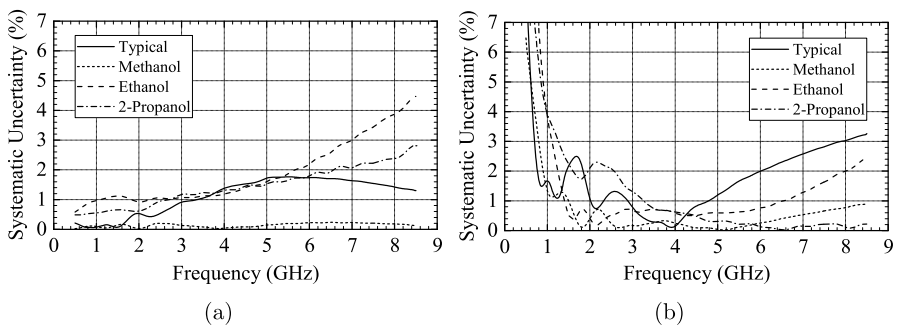

FIGURE 8.6

Systematic error (%) in the measurement of the DMSO (equivalent to high water-content human tissues) with different calibration setups: a) dielectric constant, b) loss factor.

As mentioned before, the Gabriel's database [Gab96] is the most widely used reference for test and evaluation of wireless devices operating in the vicinity of the human body tissues. However, one major issue with this database is that the reported results are obtained from different experiments, animal specimens, and measurement techniques. Therefore, direct comparison between different tissues is not very suitable. Furthermore, this database only considers the average values of the

measurements, and not the variability among different measurements. Authors in [FLGPF+18] analyze this issue by reporting the mean and the standard deviation X2 (2SDM) of the complex permittivity values for several tissues at the gastrointestinal area i.e. muscle, colon serosa, fat, and skin. It was shown that the higher heterogeneity of the tissue translates into wider variability of the complex permittivity. This can be clearly observed in Fig. 8.7 where the fat tissue shows a higher variability than skin or muscle tissues. This is because the fat tissue has different content of water depending on the measurement point; thus, increasing the heterogeneity of the tissue. Such variability of the complex permittivity can have a negative impact on the communication link. For example, the antenna matching and its radiation pattern can be affected since the real values of the permittivity of the surrounding tissues are quite different than the values used during its design.

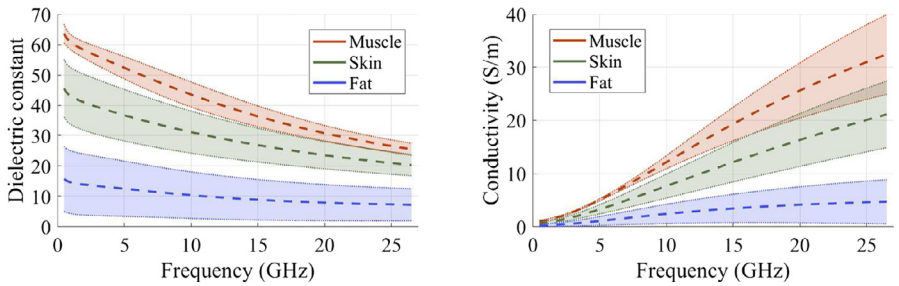

FIGURE 8.7

Mean (dashed line) and variability (shadowed area) of the dielectric properties of muscle, skin, and fat tissue.

Electromagnetic phantoms for radioelectric measurements

As mentioned before, phantoms try to replicate the electromagnetic properties of different human body tissues by using the values of the dielectric constant and loss factor given in [Gab96] or other similar databases such as [FLGPF+18]. Software or computational phantoms are computer-based models of various body tissues that can be used for electromagnetic simulations. In contrast hardware phantoms are physical materials used for experimental measurements.

Hardware phantoms (hereafter referred to as phantoms) can be solid, semi-solid, or liquid depending on the requirements of the test. Furthermore, use of phantoms is only valid for certain frequency range in which they accurately reproduce the complex permittivity of the target tissue. In the literature, there are a number of formulas for producing phantoms for many tissues and several frequency bands especially the microwave. However, it is really hard to find a common formulation for systems operating at ultra-wideband frequencies. This is due to the complexity of mimicking not only a certain value of permittivity but also its trend versus frequency. The approach reported in [CPGPFL+16] aims at overcoming this constraint by using acetonitrile-

based liquid aqueous solutions. These solutions mainly use water, acetonitrile, and salt in different proportions to replicate both the dielectric constant and the loss factor for a variety of body tissues within the 0.5 GHz to 26.5 GHz frequency band as observed in Fig. 8.8 [CPGPFL+18]. These broadband phantoms are specially appropriate to carry out physical measurements for implant scenarios. The liquid nature of the phantom allows flexibility in positioning the antenna at the desired location.

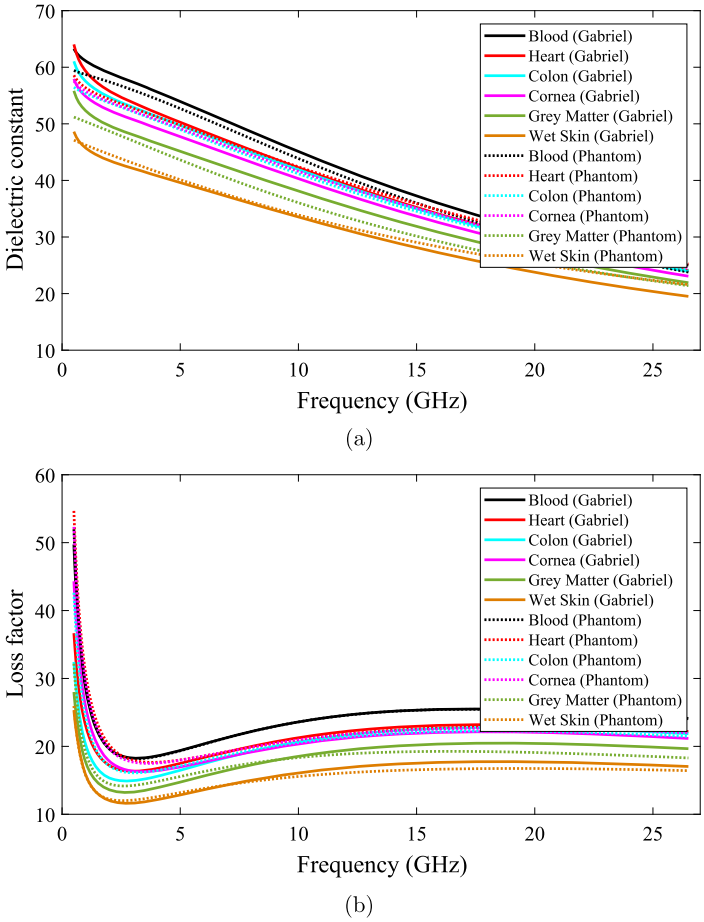

FIGURE 8.8

Relative permittivity of several phantoms (dashed lines) [CPGPFL+16] in comparison with the target values [Gab96] of their corresponding tissues (solid lines). a) Dielectric constant, b) Loss factor.

Testing radiation exposure as a result of using mobile devices is another important application of phantoms. Most of the phantoms used for this purpose are liquids applicable in a narrow frequency band. This makes testing mobile devices that use

multi-frequency technology quite difficult as multiple phantoms will be required to evaluate all frequencies under consideration. Even then, the real radiation effect would not be accurately evaluated for novel technologies such as carrier aggregation or simultaneous wireless connection. This limitation will become a real constraint for future 5G mobile systems operating in the mmWave band. In [CPGPC+18], the authors investigate a novel phantom formulation for 5G mobile communications. Due to the low penetration depth of millimeter waves, the most important tissue for the phantom is the skin. The authors analyzed propanol and methanol and concluded that propanol aqueous solutions are the best for mimicking the skin tissue for both dielectric constant and loss factor at mmWave. This level of matching can be observed in Fig. 8.9, where the shaded area depicts the ±10% deviation with respect to the mean value of the target skin tissue given in [Gab96]. The inherent heterogeneity of the tissues and variation among specimens leads to a variability in the measured values as explained before.

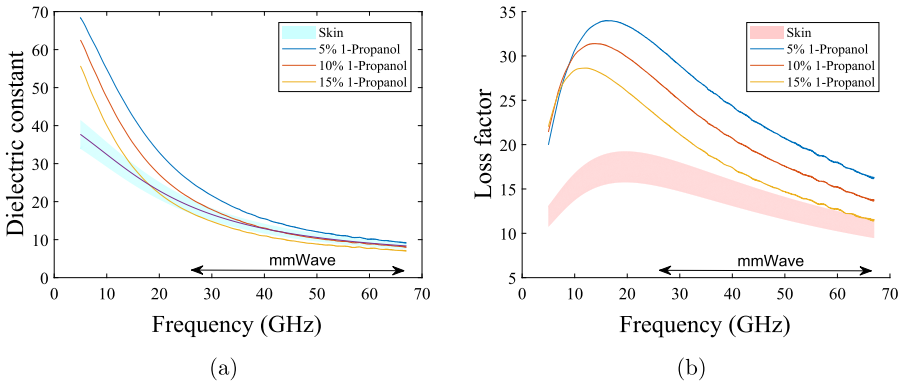

FIGURE 8.9

Relative permittivity of the k-carrageenan gels. a) real and b) imaginary part.

Human exposure to EM fields

It is known that long term exposure to EM sources could lead to several health problems [who]. Because of that there are restrictions on the maximum EM radiation enforced by national and international regulatory bodies. The EM exposure is typically limited in terms of the maximum electric field strength/power density incident on the human body or in terms of the SAR. The latter is a measure of the amount of energy absorbed by the human body when it is exposed to an EM field. SAR is expressed in watts per kilogram. The exposure limits and SAR also depends on the dielectric properties of the human tissues; and therefore, on the frequency under study.

The evaluation of the SAR resulting from a Personal Wireless Communication Device (PWD) is a challenging task due to its operation in the close vicinity of the human body. Accurate computational estimation of the SAR for such devices will

be critical to ensure adherence to national or international safety limits. Therefore, near-field validation of the numerical models used for SAR computation becomes necessary. In [HBPH17], authors present a novel validation technique based on the comparison of measured and simulated one-port characteristics of the PWD antenna while the near field is systematically perturbed by a dielectric control object near the PWD. In particular, the authors use the input impedance Z as a single-port parameter and propose a formula for the change of the antenna impedance in the near field, as well as a formula that relates the error of such changes to the near field values. Using these formulas, authors numerically verify the equivalence of the two near-field validation techniques by comparing measured and computed validation data for a Planar-Inverted F Antenna (PIFA) as observed in Fig. 8.10. After applying a deconvolution directly to the values of the impedance changes and considering Tikhonov regularization of the convolution kernel, the reconstruction of the 3D electric field with reduced error will be possible. Further technical details can be found in [HBPH19].

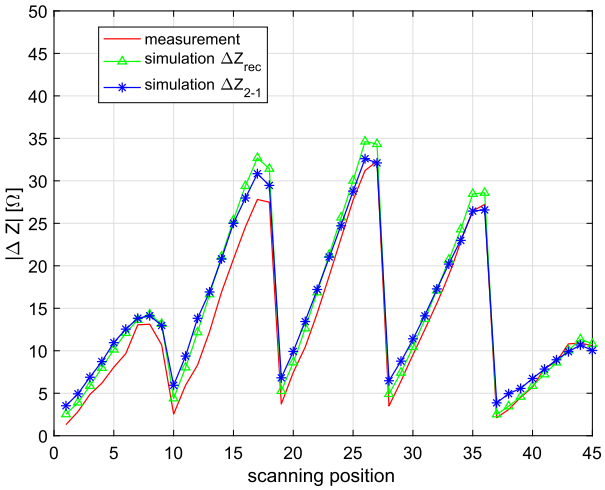

FIGURE 8.10

Comparison of the measured (red solid line; mid gray in print version), numerical impedance (green solid line with triangles; light gray in print version) from the electric field, and numerical input impedance change (blue solid line with stars; dark gray in print version).

Determination of the real exposure levels is a critical task when planning mobile communication services. In [HLHI18], authors present a large set of exposure measurements performed in different places of Kosovo. Measurements were taken for Global System for Mobile Communications (GSM), Universal Mobile Telecommunications System (UMTS), and LTE mobile technologies in DL using a commercial and calibrated spectrum analyzer. The results show that even after the implementation of LTE 1800 system (Re-farming), the main contributor to the EM exposure is

GSM 900 followed by UMTS and GSM 1800. The lowest levels of downlink base station emissions are captured from LTE. All measured values in outdoor and indoor areas (LOS and NLOS positions) are well below the International Commission on Non-Ionizing Radiation Protection (ICNIRP) reference levels [icn]. Looking at different scenarios, the highest values of the total electric field exposure were obtained in public transportation vehicles such buses, followed by coffee shops and outdoor environments. The lowest values were captured in home and office environments.

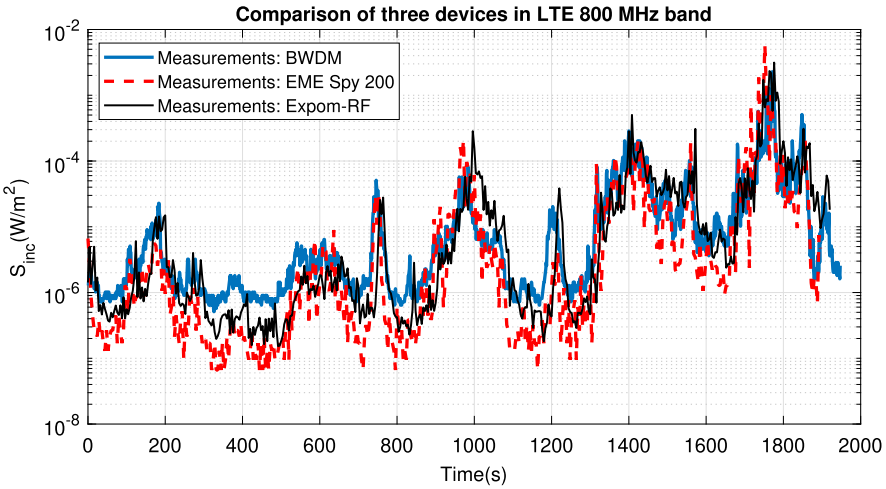

FIGURE 8.11

Incident power densities measured during the walk for several Personal Exposure Meter (PEM).

The measurement of the incident power density is conducted by the measuring (i.e. meter) device. In [ATA+18], the authors design a Multi-Band Body-Worn Distributed (BWDM) Radio-Frequency Meter as a Personal Exposure Meter (PEM). The BWDM consists of 22 textile antennas integrated in a garment covering the back and torso of the human subject. It was calibrated on 6 different human subjects and for 11 different telecommunication frequency bands. The BWDM meter has an improved uncertainty of up to 9.6 dB in comparison to commercially available personal exposure meters. Furthermore, as illustrated in Fig. 8.11, commercial PEM underestimate the exposure to EM fields when considering real measurements on a outdoor route.

8.2 IoT-health networking and applications

Future communication networks involve a plethora of 'smart' wireless devices that can exchange information in real time. These devices are expected to be part of our

daily lives, interfacing not only with humans, but also with other devices; therefore, leading to the new paradigm known as "machine to machine" communications [RRKS14]. Connected medical devices (including wearables and implants) are expected to form a smart environment capable of exchanging health information i.e. IoT-Health. The communication links in this environment can be characterized by polymorphic requirements such as latency, throughput, reliability, security, etc. [PB10]. Remote physiological monitoring is a critical application of IoT-Health which requires connectivity of wearable or implantable sensors to local or wide area networks. Remote monitoring of large numbers of patients requires sufficient bandwidth, reliable communication links and high quality of service (QoS). As part of the future 5G networks, smart medical or personal health devices operating within such environment are expected to have the capability to observe and understand the relevant physical and social parameters of their operating area. This section reports on the IRACON research activities related to IoT-health networking and applications.

8.2.1 Networking and architectures

A Body Area Network (BAN) is formally defined by the IEEE 802.15.6 standard [IEE12] as a communication and networking protocol for wireless connectivity of wearable and implantable sensors (or actuators) located inside or in close proximity of the human body. A BAN typically includes several sensor and actuator nodes along with a controller also known as coordinator. Sensors are mainly used to monitor a physiological signal while actuators apply a signal to the body or cause an operation to take place inside or on the surface of the human body. A BAN can operate as a stand-alone network or as part of a larger infrastructure. There are still several technical challenges involving implementation and integration of BANs that need to be addressed in order to achieve high reliability or Quality of Service. One such challenge is mitigating radio interference from coexisting wireless networks or other nearby BANs.

When several BANs are within close proximity of each other, inter-BAN interference may occur since no coordination across multiple networks exists in general. Authors in [BSA15] investigate the performance impact of the Energy Detection (ED) threshold within the IEEE 802.15.6 CSMA MAC protocol when the system is comprised of several co-located BANs. They have shown how the static value of this threshold can lead to starvation or unfair treatment of a particular node(s) when there are potential interferers in the vicinity. To demonstrate this, they implemented a simplified CSMA/CA protocol as outlined by the IEEE 802.15.6 standard. Same authors in [BSA16] have proposed adaptive schemes that can be used to adjust the ED threshold in the transmitting nodes of a BAN. The objective is to fairly allow channel access to all nodes regardless of the level of interference that they are experiencing. Simulation results indicate benefits of the proposed strategy and demonstrate improvement in the overall performance.

Another challenge in heterogeneous Body Area Networks is the development of methodologies for the allocation of multiple data streams with simultaneously operating radio interfaces. In [CAR+18b], authors have proposed a novel bit-rate adaptation method for data streams allocation in heterogeneous BANs. Block diagram of the proposed adaptive method is shown in Fig. 8.12. A dedicated simulator has been developed using the results of measurements in a realistic environment. Using this simulator, the efficiency of the proposed algorithm was compared with other known data stream allocation algorithms. It was shown that using transmission rate adaptation based on radio channel parameters can increase the efficiency of resource usage compared to fixed bit-rate transmissions and other algorithms.

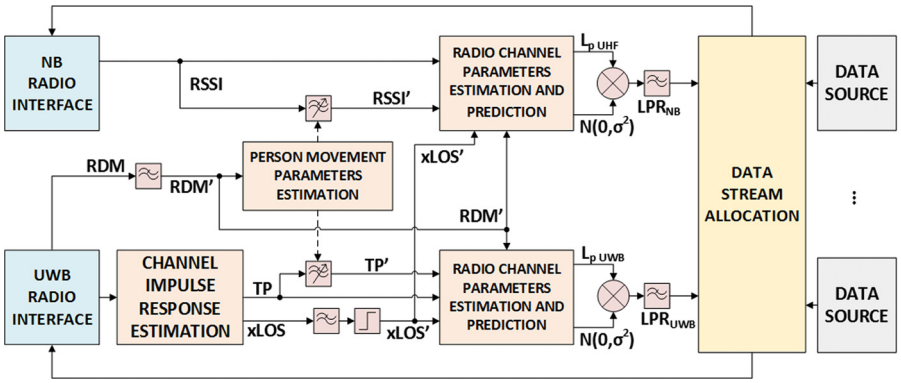

FIGURE 8.12

Block diagram of the proposed novel adaptive method for data stream allocation [CAR+18b].

Architectures for remote health monitoring

A Remote Health Monitoring (RHM) system aims to provide real-time or near real-time monitoring of patient's vital signs, thus enabling direct medical care or treatment. This technology can be used to help patients with a number of medical conditions; improving their quality of life and general well-being. It can also assist with medical and drugs' database administration. Technological advances in microelectronics, wireless communications and low-cost medical sensors are setting the stage for a 24/7 connected healthcare environment. Current medical sensors can provide a variety of physiological signals such as heart-rate, electrocardiogram, blood pressure, blood glucose levels, oxygen saturation, etc. If such sensors can be assigned a unique IPv6 address, then health information (i.e. sensors' readings) can be collected and transferred to other IP end-devices or to the Cloud for further processing and decision making.

Authors in [GFT+18] proposed the heterogeneous IoT-based architecture for remote monitoring of physiological and environmental parameters using Bluetooth and IEEE 802.15.4 standards (Fig. 8.13). The RHM system consists of a BAN with Shim-

mer physiological sensors (communicating using Bluetooth radio), and OpenMote environmental sensors communicating using IEEE 802.15.4 radio. This architecture enables data collection from multiple wearable and environmental sensors in order to process and extract useful information about the current state of the patient, as well as the environment in which the patient resides. Measurements are collected in a relational database on a local server (i.e. a Fog node for fast data analysis) as well as on a remote server in the Cloud.

Processing of the data generated by various health monitoring sensors and extracting valuable information is a complex task which requires significant resources. Authors in [TGR16] proposed a cloud-based solution to deal with this challenge. Their solution includes personalized medical devices as the source of sensor data and the cloud delivering various healthcare services over the Internet. The medical cloud hosts specially developed applications that process the data from medical devices and communicate the results to caregivers or medical institutions.

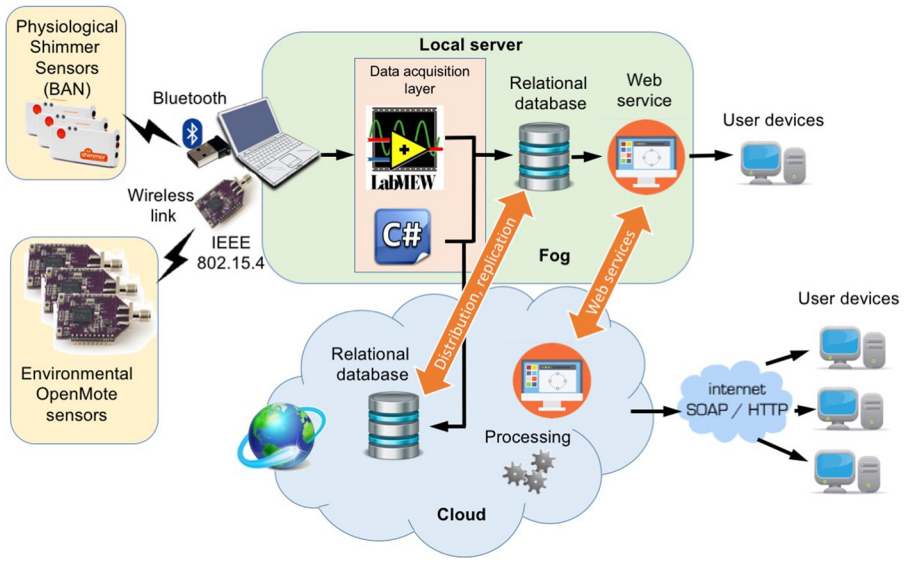

FIGURE 8.13

Heterogeneous IoT-based architecture for remote monitoring of physiological and environmental parameters [GFT+18].

Furthermore, authors in [KJD17] have provided a review on how 5G can be used as an underlying technology to provide remote health monitoring. They have also presented a novel architecture shown in Fig. 8.14. The proposed system employs White Space Devices (WSD), along with IEEE 802.22 (WiFAR) standard to provide seamless connectivity for the end-user devices. Initial findings indicate that the proposed communication system can facilitate broadband services over a large geographical area taking advantage of the freely available TVWS.

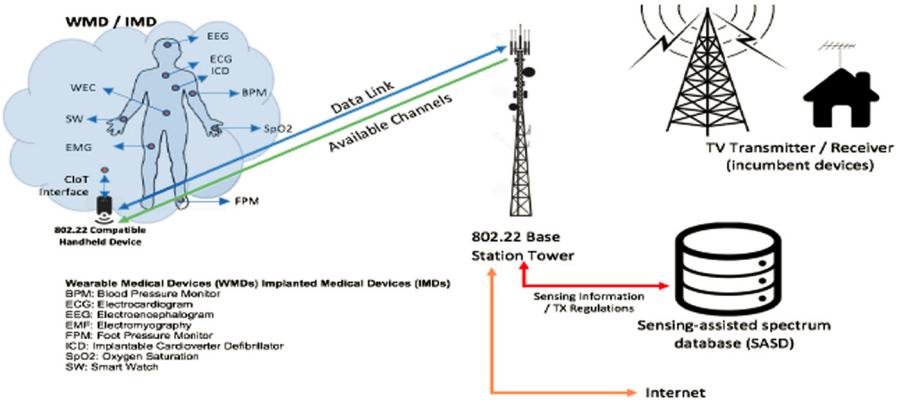

FIGURE 8.14

Proposed architecture connecting WMDs and IMDs to the internet using WiFAR (IEEE 802.22) [KJD17].

8.2.2 Applications

Localization

Localization has been mainly considered as a technology to locate objects or people in outdoor or indoor environments. However, there are new applications of this technology to locate and track indigestible electronics or capsules inside the human gastrointestinal (GI) tract. Specifically, authors in [BPG+18] explain how using UWB radio frequency transmission could be beneficial in applications such as capsule endoscopy localization. Performance analysis of RF-based localization is typically conducted through simulations using computational human body models or through experimental measurements using homogeneous phantoms. One of the most common methodologies in RF-based localization is using the received signal strength (RSS) to estimate the position of the transmitting node. Laboratory measurements using a customized multi-layer phantom test-bed [BPG+18] as well as in-vivo experiments were conducted [BGN+18] to evaluate the performance of RSS-based localization. The experimental laboratory measurements were conducted in the 3.1 GHz to 8.5 GHz UWB frequency band, and the results were used to perform two-dimensional (2D) localization. Fig. 8.15 illustrates how authors envisaged real scenarios into the phantom model that was used to conduct a number of experiments [BPG+18].

A magnetic sensor was attached to the in-body and on-body antenna so that the tracker could precisely evaluate the distance between antennas as well as their respective coordinates. Five on-body antenna positions with a separation of 2 cm along the y and z axes were considered on the outer edge of the fat phantom layer. The in-vivo measurements were conducted in a living porcine at the Hospital Universitari i Politècnic la Fe in Valencia, Spain [BGN+18] and the results were used to perform three-dimensional (3D) localization. Same antennas and equipment (Vector Network Analyzer (VNA) and magnetic tracker) were used for both in-vivo and laboratory

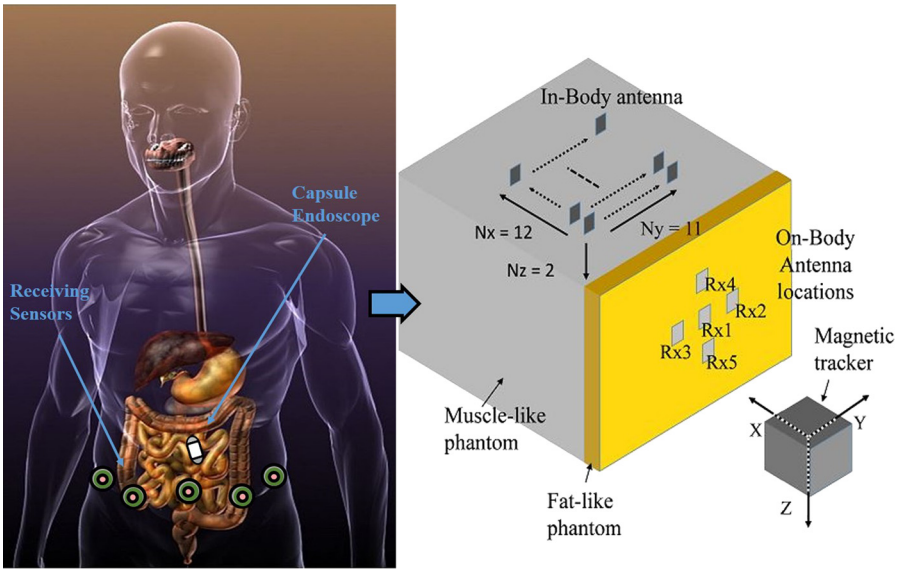

FIGURE 8.15

A multi-layer phantom-based model.

experiments. The in-body antenna was placed in three different positions inside the small bowel through laparoscopy procedure. For each in-body location, the on-body antenna was placed on the abdomen of a porcine model, and in direct contact with the skin. Measurements were taken in the 3 GHz to 6 GHz UWB frequency band, considering a resolution of 1601 points in frequency. Preliminary results on the estimation of the in-body antenna coordinates showed that RSS-based localization can achieve an average accuracy of (0.5-1) cm (assuming a limited range of distances between the in-body and on-body antennas).

Localization techniques can also be employed to locate dairy cows in a farm. In preparation for that objective, authors in [PTB+17] studied the cow's on-body and the off-body channels in both outdoor and barn environments. Bluetooth Low Energy (BLE) and UWB wireless technologies were used in that study. On-body measurements were performed in a large area of about 6 m × 12 m, so that reflections from the walls could be ignored. Path-loss measurements were performed using two ZigBee (XB24-Z7WIT-004) motes. On-body, off-body and location tracking measurement results have been presented in [BPT+16a], [BPT+16b], and [TPMJ17] respectively. The propagation path-loss for different on-body communication links on a dairy cow (ear to neck, hind leg to neck, front leg to neck, and udder to neck) has been characterized by both measurements and simulations. Measurements on a dairy cow in a multipath environment (i.e. barn) have also been performed to validate the simulations conducted using a cow body phantom. The path-loss results obtained from the simulations showed good agreement with the values derived from the measure-

ments. A log-normal path-loss model has been constructed from the measurement and simulation data for the whole cow's body.

Remote monitoring and crowdsensing

The concept of mobile crowdsensing (MCS) can be described by volunteers, equipped with sensors, who extract and share information for personal or common benefit. This concept aligns with the four pillars of the internet of everything (IoE): people, data, process, and things [SJKB19]. Initial crowdsensing typology included environmental, infrastructural, and social applications only [CCLG16], but health applications followed immediately [JS17], [PRLS15], [PRH+15], [MMA+18]. The large number of health related information, captured on a daily basis, constitutes a valuable source of diagnostic and prognostic information waiting to be explored. The hypertension is a good crowdsensing application example [JJS+18]: it exhibits no obvious symptoms and the patients tend to behave as if they were healthy. Crowdsensing can collect the location, weather condition and the cardiovascular features in order to form a large database of cardiovascular parameters in different environmental circumstances for further analysis. Patients are motivated to participate in MCS through feedback, advising them to continue or pause their current activity. The feedback is generated using the Random forest [Bre01] machine - learning algorithm, and the mean decrease impurity method for the feature importance assessment [Bre01]. The confusion matrix and the feature importance are shown in Figs. 8.16 a and b respectively. An official recommendation for MCS [GYL11] to transmit the processed features and not the complete signal initiated the development of alternative processing tools that are insensitive to artifacts in raw data. An example is Binarized entropy that estimates the approximate entropy from binary differentially coded time series [SMM+17].

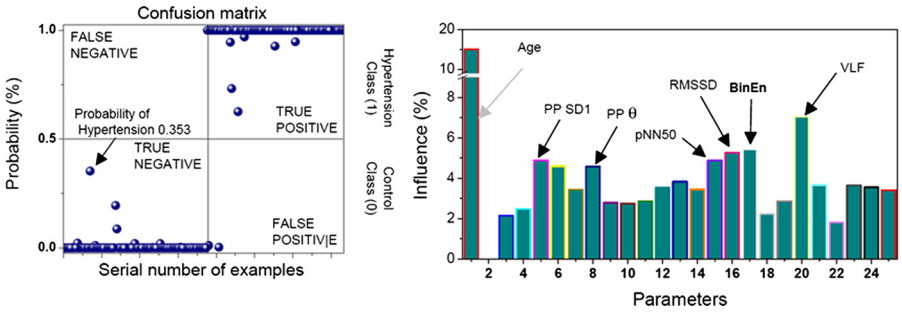

FIGURE 8.16

a) Confusion matrix; an arrow points the new patient; b) Feature importance; features are typical for cardiology; [JJS+18].

Activity recognition and motion analysis

Traditional approaches to measure a person's activity include attaching special measurement devices on predefined locations like hip and ankle. Data from those

devices are typically recorded in an internal memory for analysis at a later stage [RT12]. Many of the epidemiological and clinical studies still use this method in their research [MPGRS18]. With the advances in wearable technology, sensor measurements can be directly sent to the users' smartphone for real-time analysis. In [OR16], a system architecture for activity recognition using smartphones and smartwatches as sensor devices has been proposed. The system also includes a remote cloud which is in charge of the training and improving the neural network models used for activity recognition. Accuracy of the algorithm(s) has been evaluated to identify which sensor combination gives the best results for activity recognition. Results are shown in Fig. 8.17. The bars represent the sensors combination that have been used as input to the models. It can be seen that in general the accuracy is higher when the smartphone sensors' data is used.

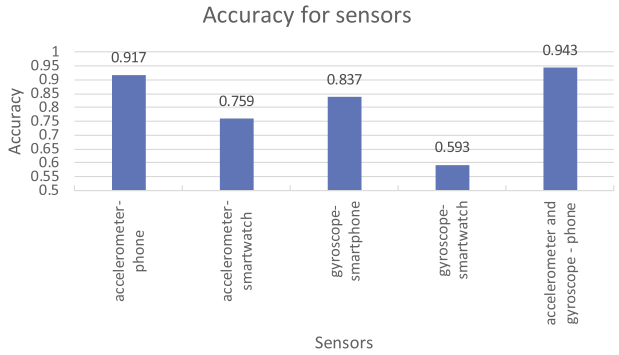

FIGURE 8.17

Accuracy for each sensor combination.

In [BPMS17], a system for remote monitoring of patients with movement disorders is presented. In addition to the system architecture, the authors describe an Android application aimed for recording of the patient's neck movements i.e. TremorSense. Initial results demonstrating the effect of botulinum toxin therapy on patients with neck tremor are shown in Fig. 8.18. The modulus of angular velocity for patient P1 before (top figure) and after (bottom figure) receiving Botulinum toxin therapy is presented in the Figure. As observed, the Botulinum toxin therapy has significantly decreased the neck tremor. This also supports the patient statement regarding an improvement on the order of 30%.

In [CAN18], authors present a low-cost portable system to capture gait signals and propose a novel method for automatically obtaining gait phases (swing and stance) using wavelets and Microsoft's Kinect RGB-D sensor. Human gait patterns are characterized by a basic gait cycle that is composed of two phases: stance and swing. Stance phase represents the state where the heel remains in contact with the ground and the swing phase represents the state where the

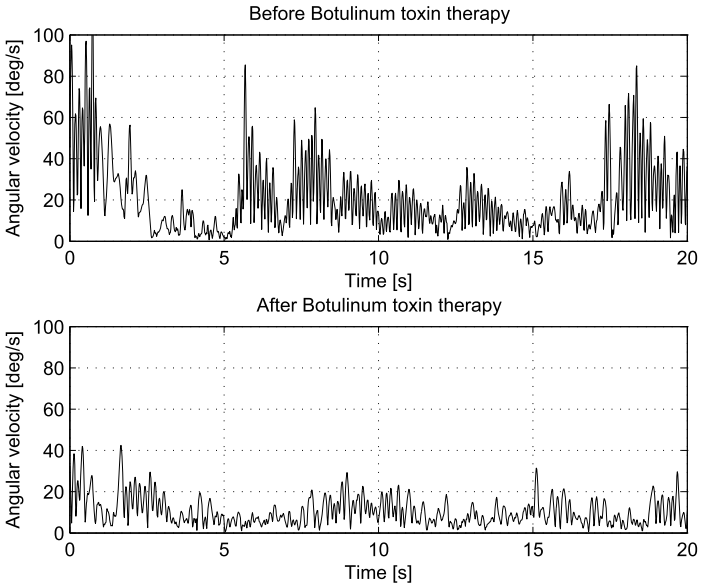

FIGURE 8.18

Angular velocity over time for patient with neck tremor.

heel moves without any ground contact. Using human gait analysis, authors derived values of spatiotemporal variables such as the walking speed, cadence, and stride length from these two phases. Table 8.7 shows how these variables clearly and quantitatively distinguish patients with Parkinson's Disease (PD). Authors explain how this approach can be used to provide an objective metric for evaluating PD progression. Furthermore, they recommend PD clinical diagnosis should include complementary gait analysis using the proposed technology.

Table 8.7 Average spatiotemporal variables and standard deviation obtained for PD and non-PD volunteers.

Variables	PD patients		non-PD patients	
	Left	Right	Left	Right
Stance Time (s)	2.24 (0.31)	2.17 (0.23)	0.91 (0.10)	1.06 (0.10)
Swing Time (s)	1.33 (0.14)	1.33 (0.18)	0.76 (0.09)	0.76 (0.06)
Step Number	10 (0.55)	9.67 (0.19)	6.83 (0.36)	6.17 (0.29)
Test Duration (s)	3.7 (0.41)	3.65 (0.32)	1.72 (0.07)	1.89 (0.09)
Speed (m/s)	0.63 (0.06)	0.65 (0.05)	1.20 (0.05)	1.04 (0.07)

8.3 Nanocommunications

The next revolutionary phase in the Internet-of-Things in healthcare is the development of nanomachines for use inside the human body. Nanomachines will enable new mechanisms for gathering information about the human health, and will open the door to innovative medical diagnosis and treatments dealing with serious infections and heart attacks [KWAC+19], vascular system diseases [KWTC19], remote surgery on an extremely small scale, drug delivery, tissues regeneration, etc. Due to their very small dimensions, nanomachines have very limited capabilities when working as a single device. This necessitates efficient cooperation of a large group of nanomachines which in turn requires exchange of information or communication among them. This is referred to as nanocommunications.

8.3.1 Nanocommunication mechanisms

In recent years, research on nanocommunications is making considerable progress along the following main three approaches: (a) EM-based, (b) molecular, and (c) FRET-based.

The first approach is based on the idea of continued miniaturization of the existing microelectronic devices. These miniaturized devices, which are expected to operate in the THz band (0.1 THz to 10 THz), are made of new materials such as carbon nanotubes or graphene. The wavelength of the EM waves in the THz band is in the micro-meters range. This allows for the development of antennas with proper dimensions. To power EM-based nanomachines, solutions based on nanowires made of zinc oxide have already been proposed. The nanowires are able to generate electric voltage if bent or reshaped, e.g. in an environment with fluid flow. The dimensions of graphene-based devices are generally in the micro-meter range. Since their operation is still based on EM communication, they can be easily integrated with existing wireless networks in the macro scale. Consequently, they could perform as a gateway between the macro and nano devices.

The second approach to nanocommunications is based on the communication mechanisms in biology. Here, the information is not carried through the transmission of an EM wave, instead a group of molecules convey the message. These mechanisms are commonly described as molecular communication (Fig. 8.19). One example of molecular communication is calcium wave propagation using diffusion (Brownian motion) [NSM+05]. This is the mechanism commonly used for signaling between living cells. Another example is using diffusion for broadcasting larger particles (such as polymers) that carry information coded in their properly modified structure [UPA13]. In contrast to passive diffusion, some molecular communication mechanisms are based on active transportation of encoded information i.e. data can be encoded in the DNA chain of a plasmid located inside a bacterium or attached to a catalytic nanomotor [GA10]. Finally, molecular motor is another mechanism that allows carrying information encoded in the RNA (or a sequence of peptides in a vesicle), and traveling along protein tracks called microtubules [EMSO11].

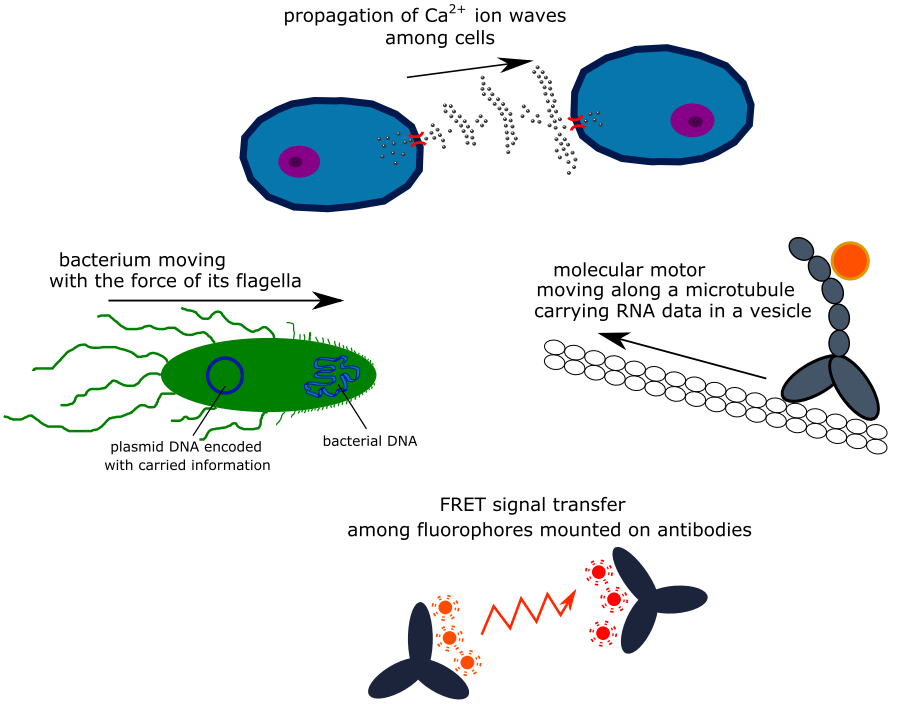

FIGURE 8.19

Examples of nanocommunication mechanisms.

The third approach to nanocommunications is based on a phenomenon called Förster Resonance Energy Transfer (FRET). This mechanism allows for non-radiative energy passing between two molecules. The first molecule, excited by an external radiation or a chemical reaction, operates as a nanotransmitter. The nanotransmitter that is in a high energy state may pass its energy to a neighbor molecule, operating as a nanoreceiver (Fig. 8.19). The phenomenon of FRET occurs only between spectrally matched molecules, i.e. the nanotransmitter emission spectrum should overlap the nanoreceiver absorption spectrum. ON-OFF modulation is achieved through this energy transfer between the two molecules. This means that sending an information bit '1' is realized by a FRET transfer while sending an information bit '0' does not involve any transfer of energy. FRET operates in nano scale as its communication range is usually limited to (5-15) nanometers. However, the communication efficiency is strongly dependent on the distance between the transmitter and the receiver [KKWJ17]. Similar to traditional wireless communications, FRET efficiency and communication reliability might be increased by using diversity techniques where multiple molecules operate at both sides of the communication channel i.e. MIMO-FRET. Designing routing techniques suitable for FRET-based nanonetworks is a major challenge. In [KSW17], new routing mechanisms have been

proposed based on biological properties of specific molecules like photoswitchable fluorophores, quenchers, proteins with changeable shape, and ATP synthases. FRET nanonetworks can be possibly constructed from fluorescent molecules like dyes or fluorophores, as well as, quantum dots and photosynthetic molecules of plant origin like carotenes and chlorophylls [OFK18]. Nanomaterials based on carotenes and chlorophylls might also be considered as parts of nanostructures for intelligent fabrics and materials.

8.3.2 Interface with micro- and macro-scale networks

As the communication mechanisms discussed in the previous section do not share the same physical medium, it will be really challenging to transfer data between nanomachines and other traditional wireless networks. Several solutions to this problem were investigated in [KTC19]. One such solution involves the use of channelrhodopsins molecules as nanoreceivers. Channelrhodopsins are able to create naturally occurring ion channels. After an excitation, i.e. absorption of a photon or FRET, a channelrhodopsin opens itself for at least 10 ms, creating a pore where cations (positive ions, like Ca^{2+}, K^{+}, Na^{+}) flow through. Consequently, the electrical potential behind the channelrhodopsin changes and can be measured with an electrode [KWKJ18]. This property means that such a channelrhodopsin can serve as an energy-to-voltage nano-converter. This is extremely useful for the purpose of reading FRET signals by electrical devices. Channelrhodopsin molecules might also be embedded into a nerve cell membrane replacing the neuroreceptors [KKWJ18]. When a FRET signal is received at a channelrhodopsin, cations which are flowing through the channelrhodopsin, open the pore and cause an action potential to propagate in the nerve cell. Since a single nerve cell can be over one meter long, this technique enables conversion of the FRET to electrical signals and its transmission over relatively large distances to other macro scale electronic devices (Fig. 8.20).

Transmission in FRET nanonetworks may also be initiated by devices outside the body, e.g. wearable devices in a BAN (Fig. 8.20). It can also be triggered by optically-enabled micro-size devices built from graphene. FRET nanonodes such as fluorophores can be bio-engineered molecules with distinct absorption spectra ranging from ultraviolet (380-400) nm up to infrared (700-750) nm. These molecules could be used for selective reception of optical signals coming from other micro/macro devices.

Communication between different types of nanonetworks (namely FRET and molecular), although challenging, is possible as well. Molecular motors such as kinesins or dyneins may not only carry information encoded in the RNA, but also fluorophores (Fig. 8.20). Depending on the actual location of the carried fluorophore, such mobile fluorophores could forward a signal to different remote FRET networks. The signaling mechanism in FRET typically starts with a nanotransmitter excited by a photon. However, a chemical reaction can also initiate the delivery of the required energy. This process is referred to as Bioluminescence Resonance Energy Transfer (BRET). For this chemical reaction to occur, luciferin (substrate), luciferase

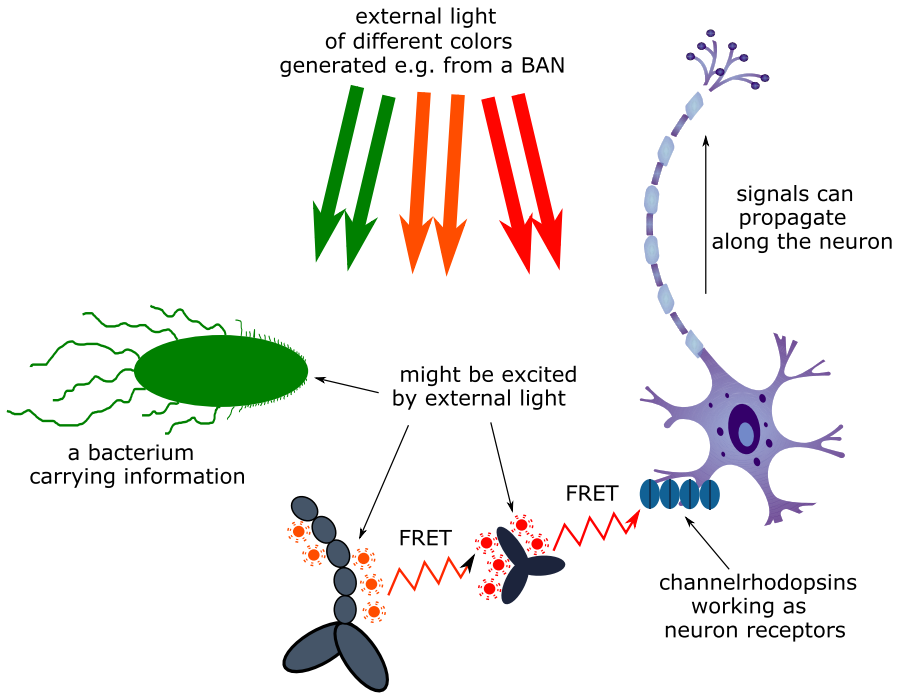

FIGURE 8.20

Communication mechanisms between the molecular/FRET networks and external devices.

(enzyme), oxygen, and ATP (energy source) are required. The process of energy delivery may also be controlled by molecular mechanisms. For example, the oxygen flow could be regulated or ATP could be transported in vesicles or molecular motors.

Finally, micro-size mobile nodes using THz communication can be used to interface with mm-scale static gateways using classical wireless communications [KWAC+19]. However, this connection is limited to distances of several millimeters due to large signal attenuation by the human tissues as well as possible regulatory limitation on the transmit power.

Methodologies discussed in this subsection show alternative mechanisms that can be used to create efficient interfaces between nano-, micro-, and macro-communication networks. These interfaces are clearly essential to realize the full potential of such integrated networks and support future technological advances in various IoT-Health applications.